Near-field scanning optical microscopy to study nanometric structural details of LiNbO$_3$ Zn-diffused channel waveguides

J. Canet-Ferrer,[1,a)] J. Martinez-Pastor,[1,b)] E. Cantelar,[2] F. Jaque,[2] J. Lamela,[2] F. Cussó,[2] and G. Lifante[2]

[1]*Instituto de Ciencia de los Materiales, Universitat de València, P.O. Box 22085, 46071 Valencia, Spain*
[2]*Departamento de Física de Materiales, C-IV, Universidad Autónoma de Madrid, 28049 Madrid, Spain*

A near-field scanning optical microscope (NSOM) is used to perform structural and optical characterization of the surface layer after Zn diffusion in a channel waveguide fabricated on lithium niobate. A theoretical approach has been developed in order to extract refractive index contrast from NSOM optical transmission measurements (illumination configuration). As a result, different solid phases present on the sample surface can be identified, such as ZnO and ZnNb$_2$O$_6$. They appear like submicrometric crystallites aligned along the domain wall direction, whose origin can be ascribed to some strain relaxation mechanism during the annealing process after Zn diffusion. © *2008 American Institute of Physics*. [DOI: 10.1063/1.3000464]

I. INTRODUCTION

Nowadays, lithium niobate (LN) crystals doped with rare earth ions are employed in many applications on laser technology and optoelectronics.[1–3] Nonlinear optical processes can be enhanced on such crystals by guiding light into metal-diffused planar channel waveguides[4–6] giving rise to novel photonic devices in the field of integrated optics, telecommunications, and biosensors.[7–9] However, some important microscopic aspects closely related to the technological development of the optical guides (and therefore essential in order to optimize their design parameters) are still unknown at nanometer scale, as for example the spatial distribution of metal diffused deep into the bulk substrate.

The near-field scanning optical microscopy (NSOM) technique has been recently probed to be useful in the study of domain walls in different nanostructured ferroelectric materials.[10–12] In this work, the NSOM technique is used to extract structural and optical information of Zn-diffused channel waveguides in LN with subwavelength resolution. We are interested in the study the Zn-rich upper layer formed from the solid solution after diffusion process[13] and also its possible influence in the light confinement at the waveguide. The Zn contained in such a layer is due to the presence of ZnNb$_2$O$_6$ and ZnO phases, as revealed by x-ray diffraction measurements.[14] These materials at the channel surface are observed at nanometer scale by NSOM due to optical transmission contrasts. They appear like submicrometric crystalline features aligned parallel to the ferroelectric domain structure that suggests a correlation with strain relaxation mechanisms at the domain walls occurring during the Zn-diffusion process. A two-dimensional (2D) model has been developed in order to transform such optical contrasts into refractive index contrasts. This model serves us to distin-guish semiquantitatively the optical contrasts produced by ZnO and ZnNb$_2$O$_6$ nanocrystalline phases on the Zn-rich upper layer above the channel waveguide.

II. EXPERIMENTAL

The sample studied in this work consists in a LN *Y*-cut wafer grown by the off-centered Czochralski method, codoped with erbium and ytterbium and presenting inverted aperiodical ferroelectric domains (Z^+ and Z^-). The angle between the domain walls and the *X*-axis in the *Y*-face is 52.25°, which corresponds to the angle produced by the projection of the [010] vector (of the hexagonal unit cell) onto the plane *Y* with the [100] direction.[15] Several waveguides 1–20 μm wide were patterned along the *X*-direction by using UV lithography on a 1 μm thick SiO$_2$ mask deposited on the LN wafer. The method of making the Zn-diffused channels is a two-step process, exchange and diffusion, as explained in Ref. 16. The refractive index contrast between the guides and the host LN is determined by the creation of solid solution regions based on zinc niobate, with a negligible contribution of the Er:Yb doping.[4] As aforementioned, before the thermal treatment, x-ray analysis revealed the presence of a ZnNb$_2$O$_6$ phase on the planar waveguides. Furthermore, after the annealing in air (last process of the waveguide fabrication) such phase was accompanied by a ZnO one.[14] In the present work, we are interested in obtain the shape and distribution of these two phases by using NSOM since their morphology is key for comprising the Zn-diffusion process and the waveguide formation mechanisms. For this purpose, the topographical profile of the SiO$_2$ mask is useful in order to identify the waveguide channels and also to place the NSOM tip onto their surface, as shown in Fig. 1.

Our NSOM is based on a tuning-fork quartz sensor head (AttoNSOM-III from Attocube Systems) controlled by an adapted commercial feedback electronics and data acquisition (Nanotec Electronica S.L.). The control of the shear force motion of the tuning-fork can be used to register a

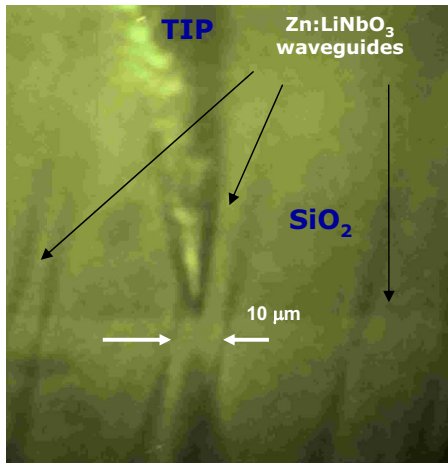a)Electronic mail: jose.canet-ferrer@uv.es.
b)Electronic mail: martinep@uv.es.

FIG. 1. (Color online) NSOM tip onto a 10 μm wide waveguide. The SiO$_2$ mask is very useful in order to place the NSOM tip at the desired measuring zone.

topographic image that can be compared with the optical one.[17] The sample surface is illuminated by coupling different diode lasers to the optical fiber probe (illumination configuration[18]) and the transmitted light is measured by a Si detector located below the sample holder. An appropriate excitation wavelength above the cutoff frequency of the probe tip was determined to be around 660 nm because of the enhancement of the refractive index contrast over topographical features.[11]

III. NEAR-FIELD OPTICAL STUDY OF THE WAVEGUIDE UPPER LAYER

A. 2D model for NSOM optical transmission

Optical images acquired by NSOM can be treated by means of theoretical calculations in order to extract all the information they contain, but unfortunately, there is not a user friendly analytical expression to describe transmitted signal under near-field conditions through a sample whose surface exhibits a random roughness having lateral dimensions comparable to the NSOM tip. In this sense, the task of reproducing a refractive index profile of surface and subsurface objects from optical transmission contrasts requires a great calculation effort to obtain accurate quantitative results. In addition, the surface characteristics of a waveguide channel present other difficulties to perform an accurate estimate of optical contrasts, since some parameters (index profile, channel size, etc.) are not well known. However, we just need to discriminate between different phases of the waveguide upper layer to understand the dynamics of the Zn-diffusion process, as aimed in this work. In this sense, NSOM transmission images could be easily interpreted if we take the next considerations in a 2D model: (i) the sample is considered a flat surface multilayer with a determined effective refractive index at the surface, (ii) a different effective refractive index is considered at the upper layer depending on the tip position (i.e., at each pixel of the image), and finally, (iii) the electromagnetic field distribution in the plane of the probe aperture is approached to a Gaussian spatial distribution with a standard deviation $\sigma \sim 80$ nm (i.e., ap-
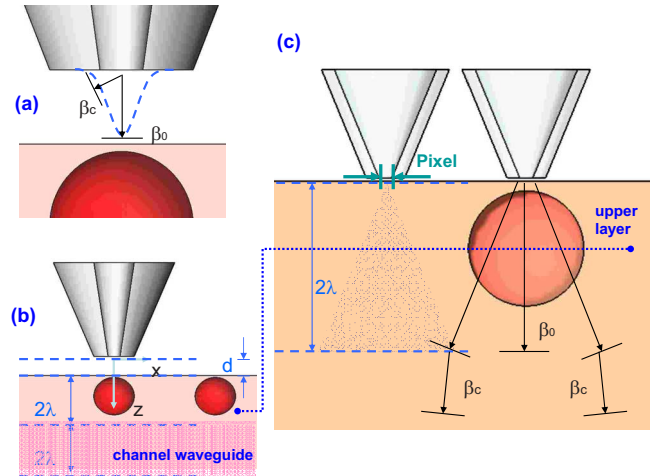

FIG. 2. (Color online) (a) Near-field probe close to the feedback range. The optical intensity on the aperture plane is approached to a Gaussian field distribution. (b) Scheme of the different layers considered in our 2D simulation. Working at constant gap mode the tip is maintained at a distance d of a few nanometers. The upper layer is considered as a flat film (2λ thickness) with an average refractive index $n_{\mathrm{eff}}(x,y)$, which depends on the position. The channel waveguide is considered as a deeper homogenous film with a larger refractive index n_{channel}. Below the channel waveguide (really located at a far-field distance), we finally find the LN substrate having the refractive index $n_s = 2.2$. The pictures are not at a correct scale in all dimensions. (c) 2D representation of the near-field probe (80 nm) in feedback range close to a scatter object larger than the wavelength (900 nm). The relative position of the propagating light cone and the sphere immersed in the Zn-diffused upper layer depends on their optical convolution. Therefore, a different effective refractive index n_{eff} is expected for each pixel of the NSOM tip scan.

proximately the tip aperture diameter), as illustrated in Fig. 2(a). Taking into account these considerations the light transmission contrasts can be simulated as follows.

First, the electromagnetic field distribution coming from the optical probe is decomposed into its angular spectrum,

$$E(x,z=0) = \sum_{\beta=-\pi/2}^{\beta=\pi/2} c^{(\beta)} e^{k_x x}. \qquad (1)$$

This way, the excitation light is developed into a linear combination of plane waves simplifying the calculations since the transmission for each component can be treated separately.[19] Such decomposition consists of a 2D Fourier transform of the propagating and evanescent plane waves,

$$c^{(\beta)} = \sigma\sqrt{2\pi} \int e^{-\frac{1}{2}\left(\frac{x}{\sigma}\right)^2} e^{-k_x x} dx, \qquad (2)$$

where k_x is the projection of the wavenumber along the X axis and $\beta = k_z$ is the wavenumber corresponding to the propagation direction [see Fig. 2(a)]. The plane waves propagate in free space from the tip to the sample surface [i.e., a typical air gap of 10 nm under feedback conditions, represented by the distance d in Fig. 2(b)]. At this point, reflection at the surface (and later at rest of layers) is considered according to condition (i) and beneath it, the plane-wave components propagate through an inhomogeneous medium (the sample upper layer). As an approach, the light transmission is calculated in an effective medium approximation [condition (ii)], due to the presence of crystalline nanospheres (hav-

ing a diameter of the order of the light wavelength) in a host matrix medium, both having different a refractive index values. The transmission of each plane wave at the sample surface is calculated by using the boundary conditions of Maxwell equations between two dielectric media,[20]

$$T_{\text{eff}}^{(\beta)} = [t_{\text{eff}}^{(\beta)}]^2 = \left| \frac{E_{\text{eff}}^{(\beta)}(x, z = d)}{E_i^{(\beta)}(x, z = d)} \right|^2. \tag{3}$$

Notice that if a suitable reference plane is chosen for the angular spectrum decomposition, the transmission for each incident plane wave $E_i^{(\beta)}$ would correspond to the Fresnel coefficient at the incidence angle

$$\theta_i = \text{arc}\sin(k_x/n_i k_0), \tag{4}$$

which is related with the β-wavenumber by

$$\beta_i^2 = n_i k_0^2 - k_x^2, \tag{5}$$

while the angle of the transmitted wave can be directly obtained from the Snell's law[20]

$$\theta_{\text{eff}} = \text{arc}\sin\left(\frac{n_i}{n_{\text{eff}}} \sin \theta_i \right). \tag{6}$$

Once the light crosses over the upper layer [with a typical thickness in the range $1-2$ μm (Ref. [13])], it suffers a second reflection (and refraction) at the homogenous channel waveguide layer. Expressions like Eqs. (3)–(6) can be deduced again to determine the transmission coefficients through the channel waveguide plane; however, in this case, the incidence angle corresponds to the inclination of waves in the effective media θ_{eff},

$$T_{\text{channel}}^{(\beta)} = [t_{\text{channel}}^{(\beta)}]^2 = \left| \frac{E_{\text{channel}}^{(\beta)}(x, z = d + 2\lambda)}{E_{\text{eff}}^{(\beta)}(x, z = d + 2\lambda)} \right|^2. \tag{7}$$

The real thicknesses of the upper layer and the waveguide are not known, but exact values are not indispensable for the semiquantitative discussion aimed in this work. These parameters just affect the phase of electric field amplitudes, but not to transmittances T_{eff} and T_{channel}. Nevertheless, it is necessary to point out that the thickness of each layer must be taken into account in certain important cases, like in very thin films (thickness $\ll \lambda$) and stratified media (including microcavities) based on them, for which multiple reflections are expected to contribute significantly. For simplicity, we will assume both thicknesses to be 2λ, as indicated in Fig. 2(b), which should not be far from actual values. Finally, the transmission at the interface between the channel waveguide and the sample substrate will be

$$T_s^{(\beta)} = [t_s^{(\beta)}]^2 = \left| \frac{E_s^{(\beta)}(x, z = d + 4\lambda)}{E_{\text{channel}}^{(\beta)}(x, z = d + 4\lambda)} \right|^2, \tag{8}$$

and the light arriving to the photodetector will take account of the last substrate-air interface,

$$T_{\text{air}}^{(\beta)} = [t_{\text{air}}^{(\beta)}]^2 = \left| \frac{E_{\text{air}}^{(\beta)}(x, z)}{E_s^{(\beta)}(x, z)} \right|^2. \tag{9}$$

In this last interface, plane waves arriving with an incidence angle larger the critical one for total internal reflection θ_{tir} will not contribute to detected light. At the same time, the finite dimensions of the detector must bee also taken into account since the numerical aperture (NA) of the photodiode could introduce another limiting angle. Indeed, we can define a cutoff wavenumber, $\beta_c = \text{NA } k_0$ like the maximum wave vector of the measurable light, which is equivalent to a maximum receiving angle θ_c by the relation $\beta_c^2 = n_i k_0(1 - \sin^2 \theta_{\text{cut}})$,[21] limited by either the detector or total internal reflections. Finally, the light arriving to the detector can be written as

$$T = \sum_{-\beta_c}^{\beta_c} T_{\text{air}}^{(\beta)} T_s^{(\beta)} T_{\text{channel}}^{(\beta)} T_{\text{eff}}^{(\beta)} |c^{(\beta)}|^2. \tag{10}$$

B. Effective medium approximation

It is necessary to point out that according to condition (ii), the effective refractive index is going to depend on the upper-layer local composition. Therefore, a different refractive index must be considered at each measuring point (at each pixel of the transmission image). Figure 2(c) illustrates how the local refractive index is estimated in this work. It is based on the effective medium theory, which recently has been successfully applied to ferroelectric materials.[22] The effective dielectric constant ε_{eff} (and therefore the refractive index) for a D-dimensional composite (in our case we limit the model to $D = 2$) comprising nanocrystals with permittivity $\varepsilon_{\text{nano}}$ and a filling factor p with respect to the host medium (the upper layer) with a permittivity ε_{up} is given by[23]

$$\varepsilon_{\text{eff}} = \frac{1}{2(D-1)} \{ (Dp - 1)\varepsilon_{\text{nano}} + (D - 1 - Dp)\varepsilon_{\text{up}} + \sqrt{[(Dp - 1)\varepsilon_{\text{nano}} + (D - 1 - Dp)\varepsilon_{\text{up}}]^2 + 4(D-1)\varepsilon_{\text{nano}}\varepsilon_{\text{up}}} \}. \tag{11}$$

As a difference, we just consider the area corresponding to the light cone cross section limited by the detector and, consequently, the filling factor is determined with respect to such area, as indicated in Fig. 2(c) (i.e., the isosceles triangle determined by β_c).

The calculation of the refractive index when scanning the surface of the waveguide upper layer by the NSOM tip is based on the convolution between the propagating light cone [triangular section depicted in Fig. 3(a)] and nanocrystalline phases [900 nm diameter nanosphere in Fig. 3(b)]. Figures
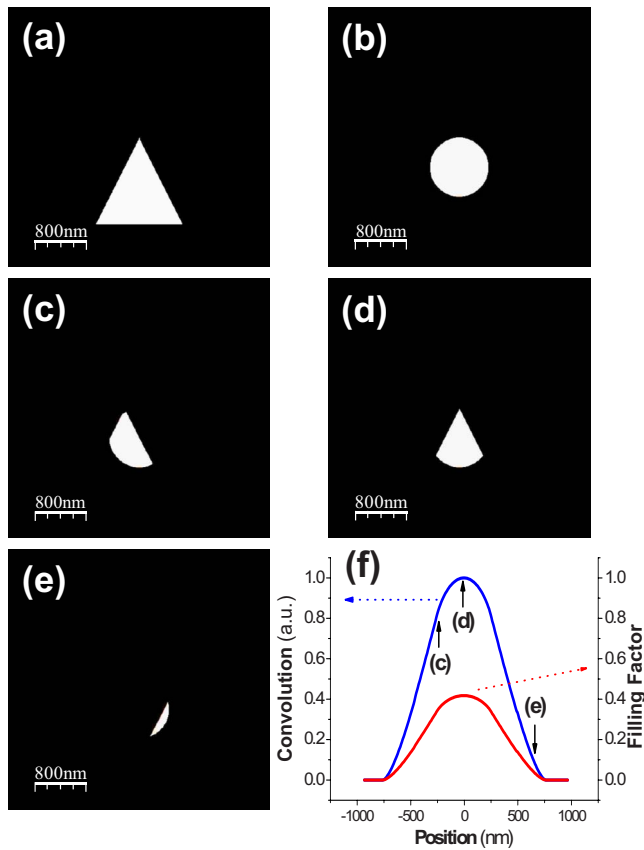
FIG. 3. (Color online) Illustration of the cross section from the convolution calculation. (a) and (b) are the 2D representations of the light cone determined by the NSOM tip and a spherical object, respectively. (c)–(e) represent the convolution when the tip is just at the left, center, and right side of the light scatterer. The area cross section and filling factor are represented in (f) in a simulated continuous scan along the X-direction.

3(c)–3(e) represent the two-dimensional (2D) cross section of the cone and the sphere when the tip is on the left, center aligned, and right side of the nanosphere, respectively. Figure 3(f) shows the complete evolution of such area (blue line) during a NSOM-tip along a scan direction (let say X) and the corresponding filling factor (red line). Obviously, both magnitudes exhibit a maximum when the tip is located on the top of the nanosphere (zero relative position).

C. Experimental results

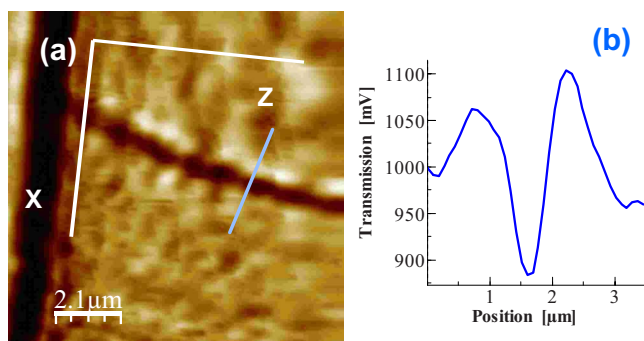Figure 4(a) shows a NSOM image with an optical dark

FIG. 4. (Color online) NSOM transmission image inside the 20 μm wide waveguide registered at 660 nm. (a) Dark linear region parallel to the domain walls whose cross-section profile is depicted in (b).

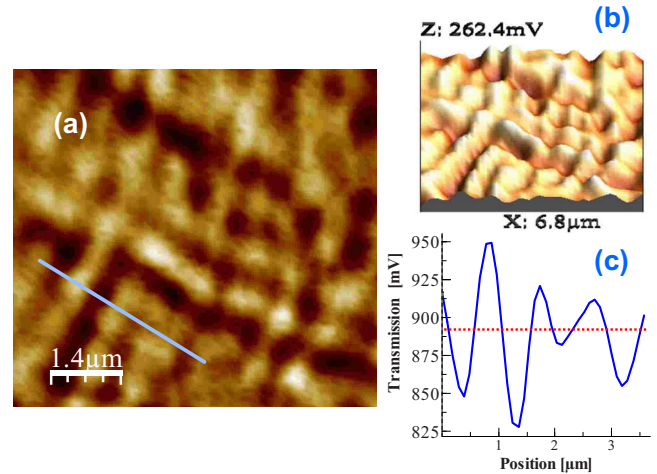FIG. 5. (Color online) NSOM transmission image inside the 20 μm wide waveguide registered at 660 nm. Nearly quasiperiodic optical contrasts parallel and perpendicular to the direction of the domain walls in 2D (a) and 3D (b) views and a typical profile (c).

contrast typically aligned parallel to the domain wall direction, sometimes surrounded by weaker bright modulations. In fact, we measure an average angle of $58 \pm 5°$ between those optical contrasts with the X direction, which coincides very well with that of the domain wall. The optical contrast across these lines can be as high as 20 %, as shown in the profile of Fig. 4(b). These elongated modulations are formed by minor ones presenting a great dispersion of size and optical contrast. In other regions of the waveguide surface, we can measure such smaller optical contrasts, which are distributed almost periodically throughout the waveguide surface, as observed in the 2D and three-dimensional (3D) images of Figs. 5(a) and 5(b). However, the period measured for these optical modulations are in the range 1.0–1.6 μm [see the profile shown in Fig. 5(c)], well below the smallest period of the domain structure (4 μm). The refractive index changes between LN inverted domains are usually between 0.05% and 0.3% (measured at the domain wall[24]), which cannot explain such huge contrasts in optical transmission images [profiles in Figs. 4(b) and 5(c)]. For this reason we attribute the observed features in NSOM images to refractive index changes between ZnO and the ZnNb$_2$O$_3$ phases present at the upper layer, as listed in Table I.

IV. DISCUSSION

We have explained above the main ingredients of our 2D model to simulate transmission profiles along a given scan

TABLE I. Measured transmission contrasts between different zones of the sample surface compared to expected values calculated by using Eq. (10) and below given refractive indices. For this table, we have used the following refractive indices at 633 nm: $n(ZnO) = 1.9$, $n(ZnNb_2O_3) = 2.3$ and n_{ave}(upper layer) = 1.98, the averaged refractive index of the upper layer (Ref. 13).

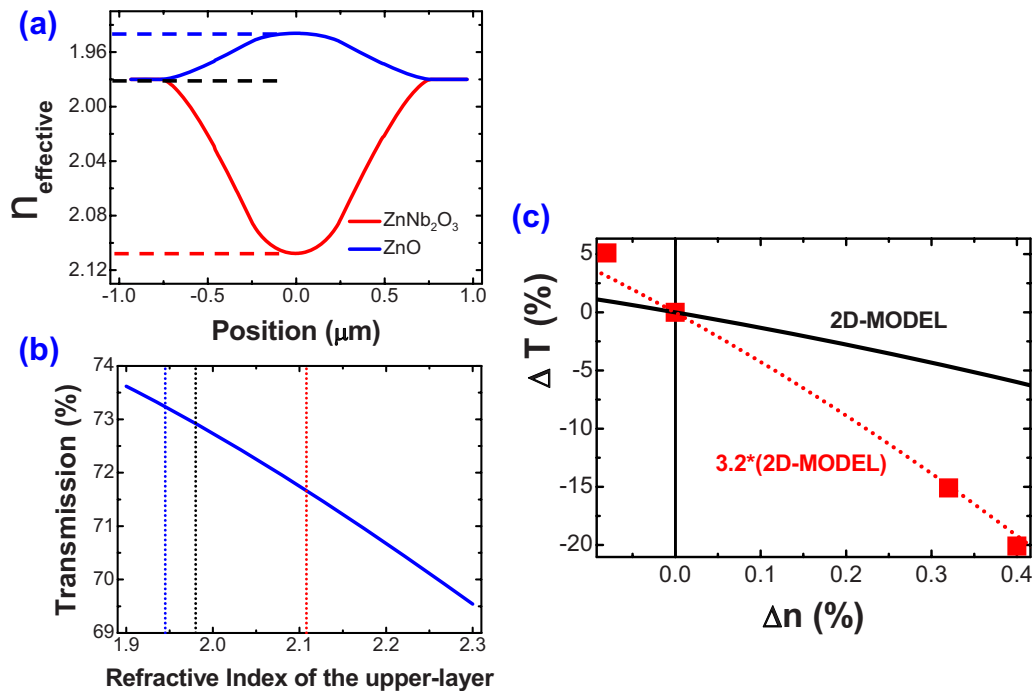| Interface	Δn	ΔT(expected) (%)	ΔT(measured) (%)
Upper layer/ZnO	−0.08	1.3	5.1
ZnO/ZnNb$_2$O$_3$	0.40	−6.1	−20.8
Upper layer/ZnNb$_2$O$_3$	0.32	−4.8	−15.5

FIG. 6. (Color online) (a) Refractive index profile expected from a ZnO (blue) and $ZnNb_2O_3$ (red) nanospheres immersed in a homogenous matrix with refractive index 1.98. (b) Transmission coefficient as a function of the effective refractive index (simulating local changes at the waveguide upper layer). (c) Comparison between experimental (red squares) and estimated (continuous black line) transmission changes for the expected refractive index contrasts at the surface of the waveguide upper layer. Dotted red line stands for calculated values multiplied by a factor 3.2 in order to match experimental values.

direction produced by an effective medium composed by nanospheres of ZnO and $ZnNb_2O_6$ immersed into a matrix material (waveguide upper layer) with an average refractive index close to 1.98, as was determined in Ref. 13. The diameter of these nanospheres is taken to be around 900 nm, as an average value obtained in several NSOM images, and the excitation wavelength is that of the experiment, 660 nm. The refractive index of the more homogenous waveguide channel (Zn solution into LN) is also taken from Ref. 13, $n_{channel} \approx 2.25$. The NSOM images have been acquired by means of a high NA detector (NA $\approx \sin 71°$) determining a limiting angle θ_c equivalent to $\theta_{tir} \approx 27°$ in LN ($n_s = 2.2$). Applying Eq. (10), we can estimate the effective refractive index profile along a given X-scan of the upper layer in which a nanocrystalline phase (ZnO or $ZnNb_2O_6$) could be present, as was illustrated in Fig. 2.

The effective media index profile produced by ZnO (blue curve) and $ZnNb_2O_3$ (red curve) nanospheres is plotted in Fig. 6(a), as a function of the tip position along a X-scan. In Fig. 6(b), Eq. (10) is used to estimate the transmission optical signal as a function of that upper-layer effective refractive index. From these calculated values, we would expect a maximum optical contrast in transmission images in the order of a 5% (see Table I) that corresponds to an alternated presence of ZnO and $ZnNb_2O_3$. However, these expected values are always smaller than the experimental contrasts, $\Delta T = (T_{pixel} - T_{average})/T_{average}$, which can reach values as high as 20%, as shown in Fig. 6(c) (red square symbols). In spite of this numerical disagreement, we observe a nearly quadratic correlation between the experimental transmission and refractive index contrasts [square symbols in Fig. 6(c)], just like predicted by Eq. (10) [continuous line in Fig. 6(c)].

This result is deduced from transmission contrast values in NSOM images by assuming that bright modulations are associated to ZnO nanocrystalline phases and dark ones to those of $ZnNb_2O_3$, as suggested by our model.

The measured experimental correlation between transmission and refractive index contrasts would coincide with the calculated one if the latter are multiplied by a suitable factor [red dotted line in Fig. 6(c) correspond to calculated values multiplied by a factor 3.2]. Such disagreement possibly would be smaller if calculations were made by using a more sophisticated and computer time consuming 3D model with an accurate selection of unknown parameters such as the local upper-layer refractive index, upper layer and channel thicknesses, nanospheres depth, etc. It is also possibly an influence of light coupling into the channel waveguide, more importantly when light impinges on phases with higher refractive index. In any case, an important semiquantitative result is that we can ascribe the low refractive index of the Zn-rich upper layer ($n_{up} \sim 1.98$) to a large content of ZnO diluted in the LN, while the quasiperiodic optical modulations along the directions parallel and perpendicular to the ferroelectric domain walls would be due to the alternate presence of $ZnNb_2O_6$ and ZnO nanocrystals. Once the $ZnNb_2O_6$ (dark contrasts) and ZnO (bright ones) phases are identified their structural characteristics can be studied. After a statistical investigation performed on several images, the average diameter can be fixed around 900 nm (as used in our simulations) with important size dispersion [see images in Figs. 5(a) and 5(b) and a typical profile in Fig. 5(c)]. The statistics show also variations in the transmission contrast mainly attributed to the size dispersion, being results shown in Figs. 4 and 5 representative of the sample.

The periodic distribution of these nanocrystals is clearly not arbitrary and could be induced by the strain field introduced by the ferroelectric domain structure. In fact, the secondary ion mass spectrometry (SIMS) measurements reported on Ref. 13 showed how the Zn-rich surface region is formed before the annealing process and how a part of this Zn diffuses until deeper regions after annealing to form the channel waveguide. Our NSOM results are in agreement with those SIMS results and, in addition, we can deduce that the Zn still remaining at the sample surface are mainly forming the aforementioned nanocrystalline phases at strained zones around the domain walls, reducing the Zn diffusion deep into the LN material.

V. CONCLUSIONS

In this work, we have studied structural and optical properties of Zn-based planar waveguides fabricated on an aperiodically poled LN crystal by near-field techniques. Transmission images have been acquired working in constant gap mode at 660 nm wavelength where it is shown that some optical contrasts were observed parallel to the interface between the inverted domains. These optical contrasts are clearly stronger than the one expected for a domain wall, and we attribute them to the presence of $ZnNb_2O_6$ and ZnO phases having sub-micrometric size. The complex sample characteristics avoid obtaining exhaustive quantitative information, even if we can identify both phases into a solid solution region by the comparison of experimental results with a 2D model to account for NSOM light transmission. As a result, an important part of the Zn at the upper layer surface above the channel waveguide is observed such as $ZnNb_2O_6$ and ZnO nanocrystals having an average size close to 900 nm. They are nearly ordered in arrays over the directions parallel and perpendicular to the domain walls, which can be driven by the accumulated stress at the domain walls.

[1] E. Lallier, Appl. Opt. **31**, 5276 (1992).

[2] D.-L. Zhang and E. Y. B. Pun, J. Appl. Phys. **99**, 023101 (2006).

[3] Y. N. Zhi, D. A. Liu, W. J. Qu, Z. Luan, and L. R. Liu, Appl. Phys. Lett. **90**, 042904 (2007).

[4] G. Lifante, E. Cantelar, J. A. Muñoz, R. Nevado, J. A. Sanz-García, and F. Cussó, Opt. Mater. (Amsterdam, Neth.) **13**, 181 (1999).

[5] E. Cantelar, R. E. Di Paolo, J. A. Sanz-García, P. L. Pernas, R. Nevado, G. Lifante, and F. Cussó, Appl. Phys. B: Lasers Opt. **73**, 515 (2001).

[6] E. Cantelar, G. A. Torchia, J. A. Sanz-García, P. L. Pernas, G. Lifante, and F. Cussó, Appl. Phys. Lett. **83**, 2991 (2003).

[7] R. C. Twu, Microwave Opt. Technol. Lett. **41**, 493 (2004).

[8] R. C. Twu, C. C. Huang, and W. S. Wang, Microwave Opt. Technol. Lett. **48**, 2312 (2006).

[9] I. Suárez, R. Matesanz, I. Aguirre de Cárcer, P. L. Pernas, F. Jaque, R. Blasco, and G. Lifante, Sens. Actuators B **107**, 88 (2005).

[10] J. Canet-Ferrer, L. Martín-Carrón, J. L. Valdés, and J. Martínez-Pastor, Bol. Soc. Esp. Ceram. Vidrio **45**, 218 (2006).

[11] J. Canet-Ferrer, L. Martín-Carrón, J. Martínez-Pastor, J. L. Valdés, A. Peña, J. J. Carvajal, and F. Díaz, J. Microsc. **226**, 133 (2007).

[12] L. Mahieu-Williame, S. Gresillon, M. Cuniot-Ponsard, and C. Boccara, J. Appl. Phys. **101**, 083111 (2007).

[13] R. Nevado, F. Cussó, G. Lifante, F. Caccavale, C. Sada, and F. Segato, J. Appl. Phys. **88**, 6183 (2000).

[14] V. A. Fedorov, Y. N. Korkishko, F. Vereda, G. Lifante, and F. Cussó, J. Cryst. Growth **194**, 94 (1998).

[15] R. S. Weis and T. K. Gaylord, Appl. Phys. A **37**, 191 (1985).

[16] B. Herreros and G. Lifante, Appl. Phys. Lett. **66**, 1449 (1995).

[17] K. Karrai and R. D. Grober, Appl. Phys. Lett. **66**, 1842 (1995).

[18] M. A. Paeleser and P. J. Moyer, *Near-field Optics: Theory, Instrumentation, and Applications* (Wiley, New York, 1996).

[19] M. Nieto-Vesperinas, *Scattering and Diffraction in Physical Optics*, 2nd ed. (World Scientific, Singapore, 2006).

[20] E. Hecht and A. Zajac, *Optics*, 3rd ed. (Addison Wesley, Reading, MA, 1997).

[21] B. Hecht, H. Bielefeldt, D. W. Pohl, L. Novotny, and H. Heinzelmann, J. Appl. Phys. **84**, 5873 (1998).

[22] V. O. Sherman, A. K. Tagantsev, N. Setter, D. Iddles, and T. Price, J. Appl. Phys. **99**, 074104 (2006).

[23] D. A. G. Bruggeman, Ann. Phys. **24**, 636 (1935).

[24] S. Kim and V. Gopalan, Mater. Sci. Eng., B **120**, 91 (2005).